aerospace

MDPI

Article

Design of High-Efficiency Jet Lift Enhancement for Flaps Under Propeller Slipstream Influence

Yan Shao [1,2], Wanbo Wang [2,*], Jiao Sun [1,*], Wenyi Chen [1], Xinhai Zhao [2] and Jiaxin Pan [2]

[1] Department of Process Equipment and Control Engineering, School of Chemical Engineering, Hebei University of Technology, Tianjin 300401, China; shaoyan2025@163.com (Y.S.); cwy63@hebut.edu.cn (W.C.)
[2] Low Speed Aerodynamics Institute, China Aerodynamics Research and Development Center, Mianyang 621000, China; 18773129527@163.com (X.Z.); panjiaxin2024@126.com (J.P.)
* Correspondence: bowanw@163.com (W.W.); sunjiao@hebut.edu.cn (J.S.)

Abstract: Both propeller slipstream and flap jet flow can significantly increase the aircraft lift coefficient. To establish design principles for efficient lift enhancement via jet flow under the influence of slipstream, wind tunnel experiments are conducted on a wing with propeller slipstream and jet flow. Force measurements using a balance and flow field measurements using hot-wire anemometry are employed to investigate the effects of different jet flow distribution methods on lift enhancement. The results indicate that the coupling of slipstream and jet flow effects can significantly increase wing lift. The stronger the slipstream effect, the more pronounced the lift enhancement under the same momentum coefficient. At the same thrust coefficient, a higher momentum coefficient is required in the slipstream-affected region to suppress airflow separation. Under the same jet flow rate, increasing the momentum coefficient in the slipstream-affected region can significantly improve lift enhancement. At the thrust coefficient of 0.46 and the momentum coefficient of 0.1, the optimized jet flow distribution method achieved a 52.6% greater lift enhancement compared to the spanwise uniform jet flow distribution method.

Keywords: jet control; flow separation; slipstream effect; hot-wire testing; wind tunnel experiment; lift enhancement

check for updates

Academic Editor: Christian Breitsamter

Received: 19 February 2025
Revised: 10 March 2025
Accepted: 11 March 2025
Published: 13 March 2025

Citation: Shao, Y.; Wang, W.; Sun, J.; Chen, W.; Zhao, X.; Pan, J. Design of High-Efficiency Jet Lift Enhancement for Flaps Under Propeller Slipstream Influence. *Aerospace* **2025**, *12*, 232. https://doi.org/10.3390/aerospace12030232

Copyright: © 2025 by the authors. Licensee MDPI, Basel, Switzerland. This article is an open access article distributed under the terms and conditions of the Creative Commons Attribution (CC BY) license (https://creativecommons.org/licenses/by/4.0/).

1. Introduction

For military transport aircraft, improving short takeoff and landing (STOL) capability enables the rapid and precise deployment of combat forces in complex battlefield environments, enhancing battlefield adaptability [1]. For civil transport aircraft, achieving short takeoff and landing can improve flight efficiency, alleviate congestion at major city airports, and reduce the runway length requirements for aircraft. It can also increase the utilization of smaller airports and help mitigate the impact of aircraft takeoff and landing noise on the surrounding environment [2]. For transport aircraft with specific STOL requirements, conventional mechanical lift augmentation systems cannot meet the design requirements for low-speed aerodynamics. The technical challenge is to achieve efficient cruising while flying slowly with smaller wing sizes during takeoff and landing, making high-lift systems a critical design target [3]. The Japanese US-2 large amphibious aircraft is a successful example of combining blown-flap technology and propeller slipstream technology [4]. Blown-flap technology, which utilizes power for lift augmentation, will play a crucial role in the design of high-lift systems for future transport aircraft [5,6].

Propeller slipstream can significantly affect the aerodynamic characteristics of aircraft tail fins and other control surfaces. Researchers have determined the interference between propeller slipstream and wings through wind tunnel experiments and numerical simulations. Alba [7] pointed out that the increase in dynamic pressure at the wing is primarily related to the axial induced velocity of the slipstream, while the change in the local angle of attack (AOA) of the wing is mainly related to the tangential induced velocity of the slipstream. Both effects alter the lift distribution of the wing. Miranda [8] utilized lifting-line theory and a vortex tube model to study the optimal design of propeller–wing configurations to reduce induced drag. Rakshith [9] et al. investigated the chord length distribution of wings under the influence of propeller slipstream. The study found that shorter chord lengths in the slipstream region are beneficial for reducing wing drag. Veldhuis [10–12] studied the twist angle distribution of wings under the influence of propeller slipstream and found that upward rotation on the inner side of the propeller, propeller installation closer to the wingtip, and higher or lower vertical positions are conducive to improving the lift-to-drag ratio. Xue Chen [13] et al. validated the accuracy of numerical methods by comparing them with experimental data. By analyzing data on the effects of different propellers on wing aerodynamic characteristics, they concluded that increasing the induced axial velocity downstream of the hub is beneficial for improving the lift-to-drag ratio. Ma Shuai [14] et al., through a combination of experiments and simulations, proposed that the enhanced dynamic pressure on the flap within the slipstream region and the high-speed slipstream have a blowing effect on the boundary layer of high-deflection flaps, which can delay airflow separation and improve flap efficiency.

With the in-depth research on active flow control technology, efforts have been made to combine propeller slipstream with active flow control for optimized design, achieving better control effects. The German Aerospace Center (DLR) [3] conducted experimental studies on the flap steady jet flow based on the Coanda effect under the influence of propeller slipstream. After control, the overall lift coefficient of the model reached 4.2, with the maximum local lift coefficient exceeding 6. The study also explored the strategy of using differential jet flow on both sides of the short nacelle to save air volume. Keller [15] and others used CFD to study the impact of jet flow flaps on aircraft's longitudinal stability, considering the effects of propeller slipstream. Murnieks [16] and others simulated aircraft's hover flight conditions and investigated the effectiveness of various trailing-edge Coanda active flow control actuators in propeller slipstream. To explore the effect of actuator design on propeller slipstream, Murnieks [17] and others also provided the optimal installation positions for Coanda active flow control actuators and compared their effectiveness in propeller slipstream. However, the effectiveness of actuators under slipstream effects with freestream flow and flaps has not been studied.

In actuator design, previous research has mostly focused on the trailing edge and the design of the wing itself, with less attention given to the design of plenum uniformly distributed along the span of the wing. J. Chard [18] and others conducted studies on the internal design of actuators. Under compact size, weight, and power constraints, they optimized the internal design from intake to exhaust using CFD to some extent and preliminarily summarized related design experiences. However, there is still a lack of systematic parametric studies and validation. Crowther B [19,20] and others conducted a parametric study on the flow distribution system of compact actuators. Through CFD and experimental verification, they analyzed the impact of the design space of each component on pressure loss and created a toolkit for designing flow distribution systems. Their approach to intake chamber design involved adding guide vanes to distribute the flow spanwise. The addition of guide vanes did have a positive effect on the spanwise distribution of

airflow, but the flow inevitably generated vortex structures at the guide vanes, increasing the complexity of the internal flow field and raising the system's pressure drop.

In previous studies, although there has been research on the coupling effect of slipstream and jet flow, most of the studies focused on the case of spanwise uniform jet flow. Murnieks [16,17] only studied the case where jet flow is present locally at the wing trailing edge without considering the effect of the freestream flow. The focus of this study is to experimentally investigate the effect of momentum variation along the spanwise position of the trailing-edge jet actuator on the propeller slipstream in the presence of freestream flow. Under the influence of propeller slipstream, the wing's upper surface is divided into two regions, the upper-wash side and the lower-wash side, using the propeller's centerline as a dividing line. The slipstream is asymmetrically distributed on both sides, with the slipstream velocity on the lower-wash side being higher than that on the upper-wash side. The overall direction of the slipstream is also biased toward the lower-wash side. The position directly in front of the propeller is where the slipstream velocity is at its maximum, and due to the influence of the propeller nacelle vortex, separation is more likely to occur at the flap. In this study, the actuator design is used to alter the local jet momentum coefficient. Through experimental methods, the effects of propeller slipstream on flap separation and jet flow control effectiveness are investigated under conditions of natural airflow.

2. Experimental Design and Methods

2.1. Wind Tunnel

The wind tunnel used in the experiment is a 0.7 m × 0.7 m tunnel from the China Aerodynamics Research and Development Center, with a dual-inlet centrifugal fan in the power section capable of reaching a flow rate of 69,700–114,800 m^3/h. The wind tunnel consists of the power section, first diffusion section, contraction section, test section, and second diffusion section. The test section is an open test section, and to optimize the experimental effect, a 0.5 m × 0.5 m tunnel body is added to form a closed test section. The stable wind speed range of the test section is 2 to 55 m/s, with turbulence intensity less than 0.3%. The inlet and outlet dimensions of the test section are both 0.5 m × 0.5 m, and the length is 0.83 m, as shown in Figure 1.

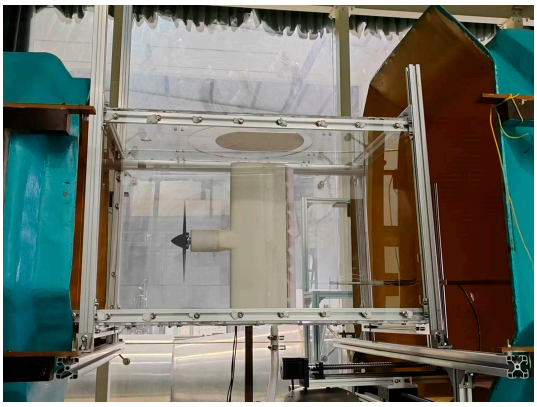


Figure 1. Wind tunnel.

2.2. Wing Model

The experimental model consists of a propeller, nacelle, main wing, and flap, as shown in Figure 2. The reference wing area is S = 0.095 m^2, with a chord length of c = 0.216 m. The increase in the flap chord length can enhance the lift coefficient, but it will also cause the blowing slot to move forward [21]. Considering the design space of the actuator and the lift improvement effect of the flap chord length, in this experiment, the flap chord length is set to 0.054 m, which accounts for 25% of the total chord length of the model. In order to

investigate the key operating conditions for short takeoff and landing or emergency lift augmentation of transport aircraft (such as the landing phase of eVTOL aircraft), where the flaps need to provide the maximum lift coefficient, flow separation control at high angles of attack is a core challenge in aerodynamic design. Therefore, the test model is selected with a fixed flap angle of 60°. The wing span is b = 0.44 m. The propeller nacelle is located at the center of the model, with a nacelle length of 0.107 m. The propeller is a three-bladed design made of carbon fiber. The spanwise length at the position directly in front of the propeller, i.e., the propeller diameter, is D = 0.2286 m, which accounts for 52% of the wing span. The jet slot is located at the starting point of the flap radius, with a slot height of 0.5 mm.

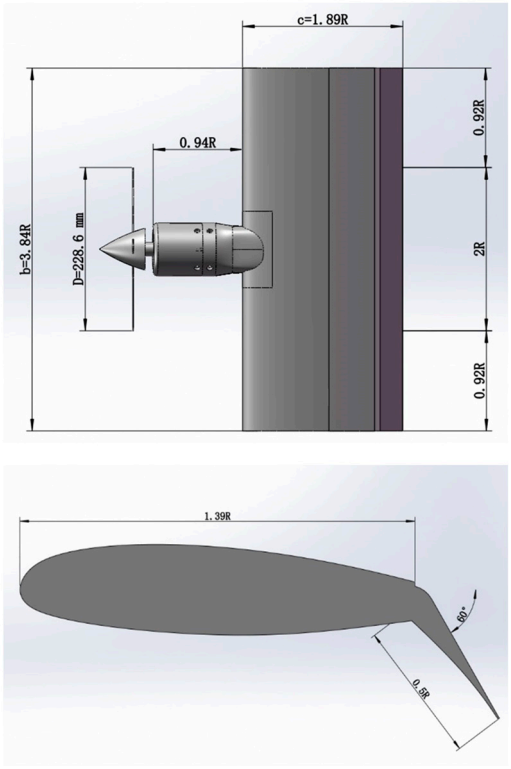


Figure 2. Model parameters.

Figure 3 shows the schematic diagram of the model's installation in the wind tunnel, with the model aligned with the center of the wind tunnel's airflow. In the experiment, the freestream velocity is set to 15 m/s. The propeller rotates counterclockwise (as viewed from the direction of the airflow). The propeller drive system mainly consists of a motor, electronic speed controller (ESC), throttle controller, and DC regulated power supply. The motor selected is a Langyu (SUNNYSKY, Zhongshan, China) Third-Generation X2820-kv1250, with a maximum continuous current of 79 A and maximum continuous power of 1172 W. Under the operating conditions of 14.8 V and 70.1 A, the thrust can reach 26.25 N. The ESC used is a Hobbywing (Shenzhen, China) Skywalker-80 A brushless ESC, with a maximum continuous current of 80 A. The throttle controller is an HJ (Huizhou, China) multifunctional servo tester, which adjusts the motor speed by controlling the output signal width, with an output signal range of 800–2200 us. The DC regulated power supply is an ANS power supply with a maximum output current of 21 A. During the experiment, the propeller thrust coefficient ($C_{T,W}$) needs to be adjusted. In order to cover the typical operating conditions of the propeller from low-load cruise to high-thrust takeoff and landing, and to reveal the quantitative impact of slipstream intensity variation on flap separation, the test selects thrust coefficients of 0.04, 0.13, 0.25, and 0.46. The propeller

thrust coefficient is calculated according to Equation (1), where T is the propeller thrust, q_∞ is the velocity pressure of the incoming flow, and S is the reference area of the wing model:

$$C_{T,W} = \frac{T}{q_\infty S} \quad (1)$$

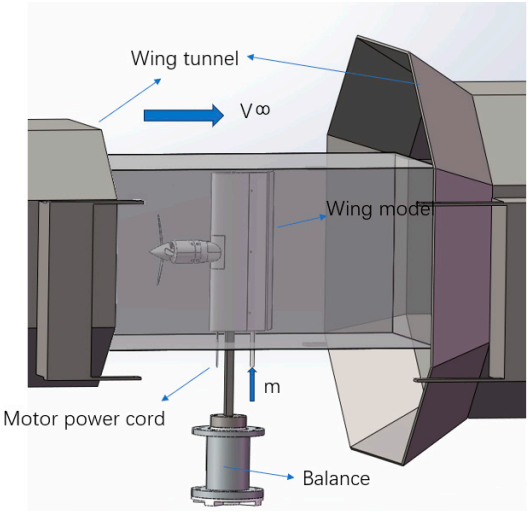


Figure 3. Model installation diagram.

2.3. Force Measurement System

The experiment uses a five-component TY02 balance from the China Aerodynamics Research and Development Center, and the balance parameters are detailed in Table 1. The wing is connected to the balance via a support rod. The balance is statically calibrated before the experiment, and the initial state is recorded. A portable PXI data acquisition system is used for data collection during the experiment, with a combined error below 0.1%.

Table 1. Performance of the TY02 balance.

Measurement Unit	Y (N)	X (N)	M_z (N·m)	M_y (N·m)	M_x (N·m)
Design load	180	35	8	35	35
Calibration load	±50	±10	±2.62	±25	±25
Absolute error	0.15	0.07	0.048	0.037	0.085
Relative error	0.2	0.2	0.05	0.01	0.02

2.4. Hot-Wire Speed Measurement System

The hot-wire measurement equipment is installed behind the wing, and its arrangement in the wind tunnel is shown in Figure 4.

The hot-wire speed measurement uses a Hanghua (Dalian, China) hot-wire anemometer CTA-04 along with its associated equipment. The hot-wire measurement system primarily includes a Hanghua hot-wire anemometer CTA-04, a Hanghua DAQ16 multifunctional data acquisition instrument, a Hanghua motor controller, a Hanghua CR04 calibrator, a mobile measurement stand, and a hot-wire probe. The CTA-04 anemometer features high-frequency response, high accuracy, and low temperature drift. The hot-wire probe uses a single wire (a tungsten wire with a length of 2 mm and a diameter of 0.5 μm). The probe is placed in a Wheatstone bridge. When the probe's resistance changes slightly due to variations in wind speed, the change in the bridge's output is amplified and alters the current flowing through the probe, which in turn suppresses the change in the probe's resistance. The instrument then records the current flowing through the heating element to obtain the variations in flow speed. The mobile measurement stand has a movement accuracy better

than 0.5 mm, enabling precise displacement of the hot-wire probe. Before the experiment, the hot wire is calibrated using the Hanghua CR04 calibrator. The calibration schematic is shown in Figure 5.

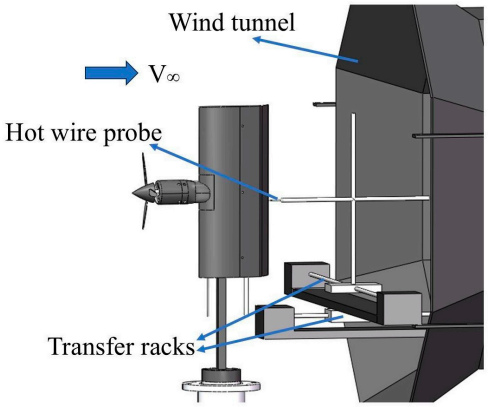


Figure 4. Arrangement of the hot-wire measurement equipment in the wind tunnel.

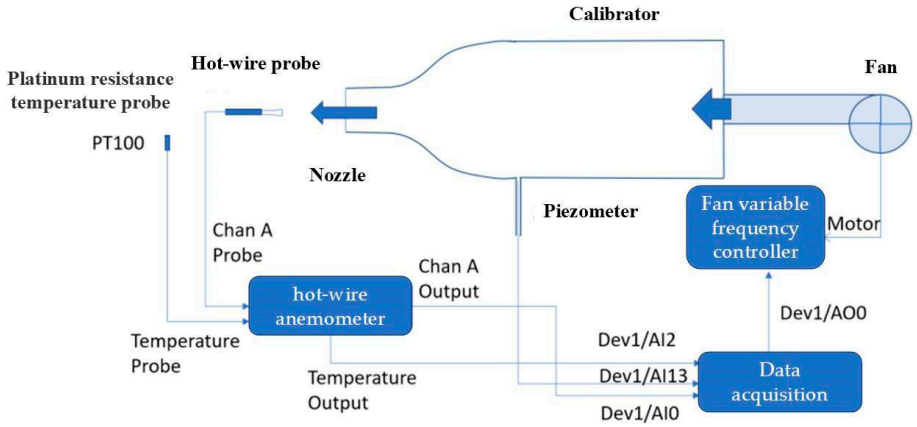
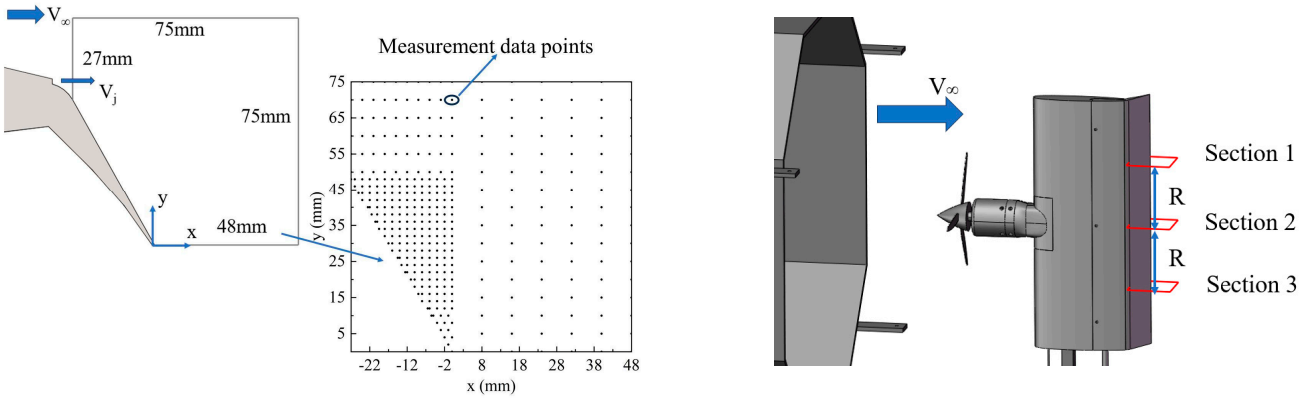


Figure 5. Schematic diagram of hot-wire calibration principle.

The range of the hot-wire measurement is shown in Figure 6a, where the reference surface at the flap is a rectangular cross section, allowing the velocity distribution at the flap to be observed. The measurement data sampling points are densely arranged near the flap, with a sampling interval of 2 mm in the dense region. A total of 356 data points are sampled throughout the entire flow field, with a sampling frequency of 10 kHz, and the sampling time for each point is 1 s. Although we used the hot-wire to measure flow separation in reverse flow areas, there are a few factors that mitigate the potential impact. First, the hot-wire probe is relatively small, resulting in a low blockage effect. Second, the data we collected are time-averaged, and the error in the hot-wire velocity measurements was verified through repeated experiments, showing that it is less than 3%. Therefore, the measured flow field data are reliable. In addition, the hot-wire experiment and the force measurement experiment were conducted independently, so the hot-wire equipment did not affect the results of the force measurements. Finally, contour velocity maps are drawn based on the sampling data. In addition, sections are measured at three different positions: the downwash side, the wing centerline (propeller center), and the upwash side, corresponding to Section 1, Section 2, and Section 3 in Figure 6b. The distance between two adjacent sections is R = 0.1143 m.



(**a**) Hot-wire measurement range. (**b**) Hot-wire measurement position.

Figure 6. Hot-wire measurement range and position.

2.5. Actuator Design

The experiment designed the actuator using a steady jet method. The schematic of the actuator can be seen in Figure 7. The actuator is divided into four parts. The blue part is the air supply pipe, with the main pipe inlet having a circular cross section of a diameter of 16 mm, distributing airflow to each branch pipe in an evenly spaced manner. To ensure that the total cross-sectional area of the branches matches that of the main pipe, 8 branches are set, with the branch cross-section designed as a circle with a diameter of 5.6 mm. The orange section is the plenum, which diffuses the airflow, and the inlet and outlet are both rectangular. Between the plenum and the branches, a smoothly transitioning circular-to-square pipe needs to be designed, which is the green part. The circular transition to the square pipe ensures that the airflow entering the inlet chamber has good uniformity and flow along the chord direction (Y-direction). After passing through the plenums, the airflow passes through a chordwise slot with a length of 1.5 mm, which is the pink part. The total chord length of the actuator is 20% of the wing's chord length. In the figure, the X-direction is the spanwise direction of the wing, and the Y-direction is the chordwise direction.

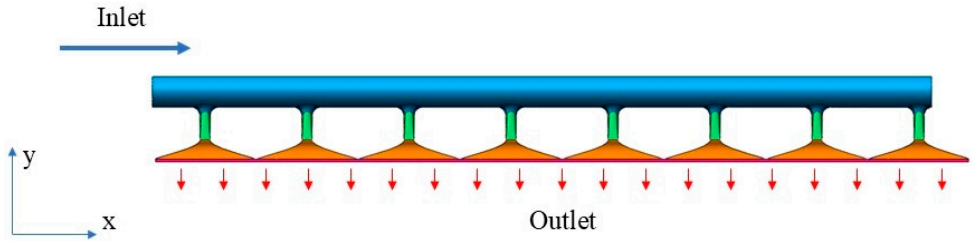


Figure 7. Actuator diagram.

To ensure the uniformity of the actuator jet flow along the spanwise direction, the plenum of the actuator is designed with an equal-area transition. The contraction curve uses a third-order Bezier curve. By designing the contraction curve in this way, it is possible to effectively eliminate the gas separation near the wall inside the plenum, achieving uniform diffusion of the airflow along the spanwise direction. The uniformity of the actuator jet flow is verified through CFD simulations, as shown in Figure 8. Under different inlet mass flow conditions, the average velocity at the outlet of each branch is nearly consistent. When the intake mass flow rate is 15 g/s, the average velocity of the 8 jet slots of the actuator is 2.7 m/s, with an error of less than 3%, confirming that the actuator has a high degree of spanwise jet uniformity.

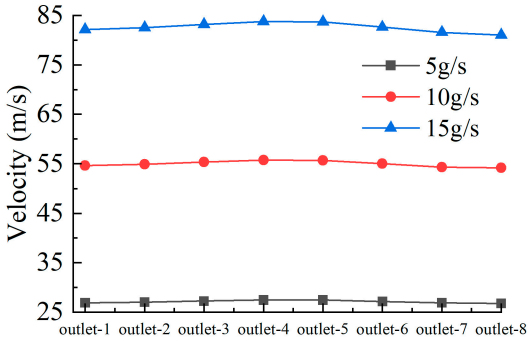


Figure 8. Average velocity at the outlet of different plenum.

To investigate the effect of different jet distribution methods on the lift enhancement under the same slipstream intensity, actuator A with a uniform jet distribution is taken as the baseline. By adding blocking designs to the jet slot exits, the areas of jet slots at different positions are varied, resulting in actuators with different effects. The design method is shown in Figure 9. Actuator A has a total of 8 plenums, each corresponding to a continuous jet slot with a length of 53 mm. After adding equidistant blocking, discrete jet slots are formed, with each block having a length of 1 mm. The area of the continuous jet slot is 1.5 times the area of the discrete jet slot.

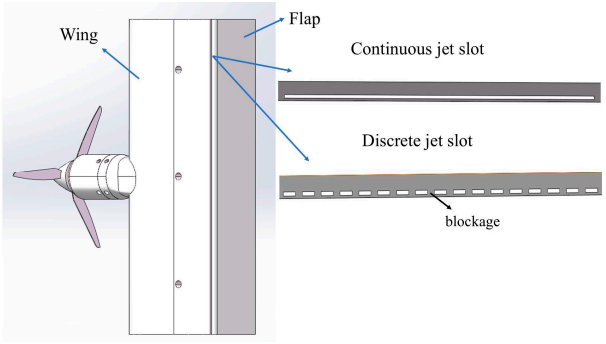


Figure 9. The jet slot of the actuator.

Figure 10 shows the distribution patterns of continuous and discrete jet slots for different actuators, where the blue represents the continuous jet slots and the red represents the discrete jet slots.

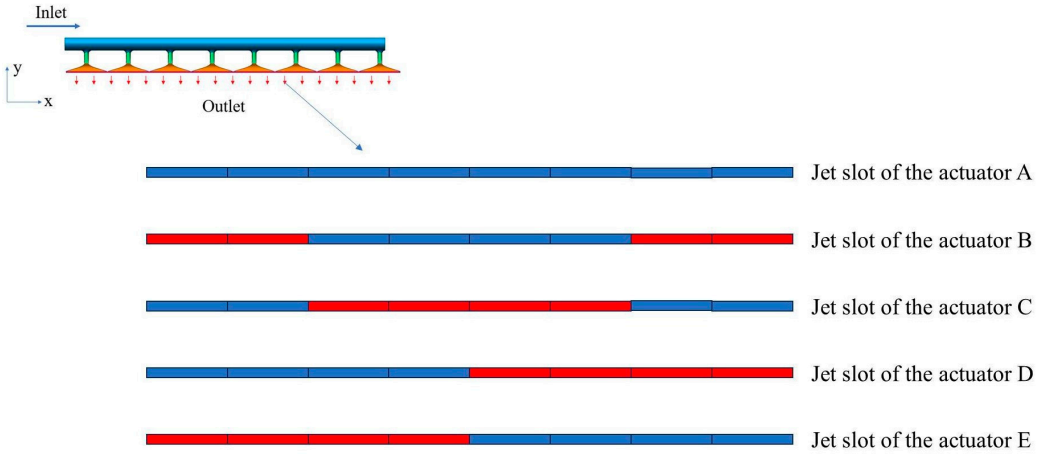


Figure 10. The distribution of continuous and discrete jet slots for different actuators.

In the experiment, the air supply for the actuator is provided by a reliable and stable high-pressure gas tank. The actuator is connected to a flow meter through a pipeline to

accurately control the airflow input, with a flow control error below 0.02 g/s. Under the assumption of neglecting pipeline losses, the jet momentum coefficient can be determined using Equation (2), where m_j is the mass flow rate of the jet, V_j is the velocity of the jet, ρ_∞ is the density of the incoming flow, V_∞ is the velocity of the incoming flow, ρ_j is the density of the jet, and S_j is the area of the jet.

$$C_\mu = \frac{m_j V_j}{\frac{1}{2}\rho_\infty V_\infty^2 S} = \frac{m_j^2}{\frac{1}{2}\rho_\infty V_\infty^2 S \rho_j S_j} \quad (2)$$

3. Experimental Data and Analysis

The test fixed wing has an angle of attack of 0°, a flap deflection angle of 60°, and a freestream velocity of 15 m/s. The propeller speed is measured using a digital tachometer, with a measurement error of less than 10 RPM. The propeller thrust and other detailed parameters are shown in Table 2. The test adjusts the jet momentum coefficient through a flowmeter, and the detailed parameters are shown in Table 3.

Table 2. Propeller parameters.

Rpm	Thrust (N)	Thrust Coefficient ($C_{T,W}$)
5380	0.51	0.04
6400	1.68	0.13
7410	3.21	0.25
8820	5.75	0.46

Table 3. Momentum coefficient.

Momentum Coefficient	Input Flow of Actuator A (g/s)	Input Flow of Other Actuators (g/s)
0.003	3.1	2.8
0.005	4	3.6
0.01	5.6	5.1
0.02	7.9	7.3
0.04	11.2	10.3
0.06	13.8	12.6
0.08	15.9	14.5
0.1	17.8	16.2

3.1. The Impact of Slipstream Effect

The impact of the propeller on the airflow over the upper surface of the wing is multifaceted. At very low propeller speeds, although the generated thrust and vortices are small, they still affect the airflow distribution on the wing surface and have a certain influence on the lift coefficient. When the freestream velocity is 15 m/s, thrust coefficients of 0.04, 0.13, 0.25, and 0.46 are selected for study. Figure 11 shows the lift coefficient curves under different thrust coefficients without jet flow. The results indicate that as the thrust coefficient increases, the lift coefficient of the wing increases approximately linearly. When the propeller thrust coefficient increases from 0.04 to 0.46, the lift coefficient increases by 37.9%. The reason for this is that as the thrust coefficient increases, the slipstream effect gradually strengthens, accelerating the airflow over the upper surface of the wing, causing the angle of attack of the wing leading edge relative to the freestream to increase, thereby enhancing the overall lift coefficient. This is consistent with the conclusions of Catalano F M et al. [22–24].

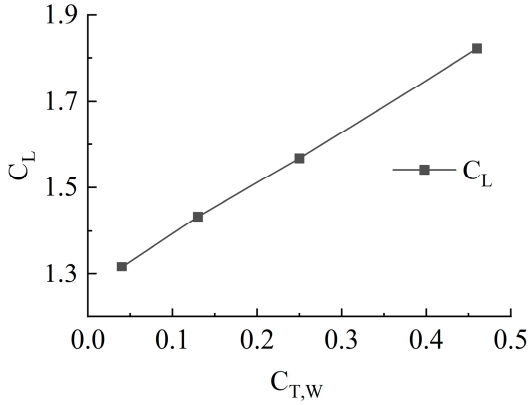
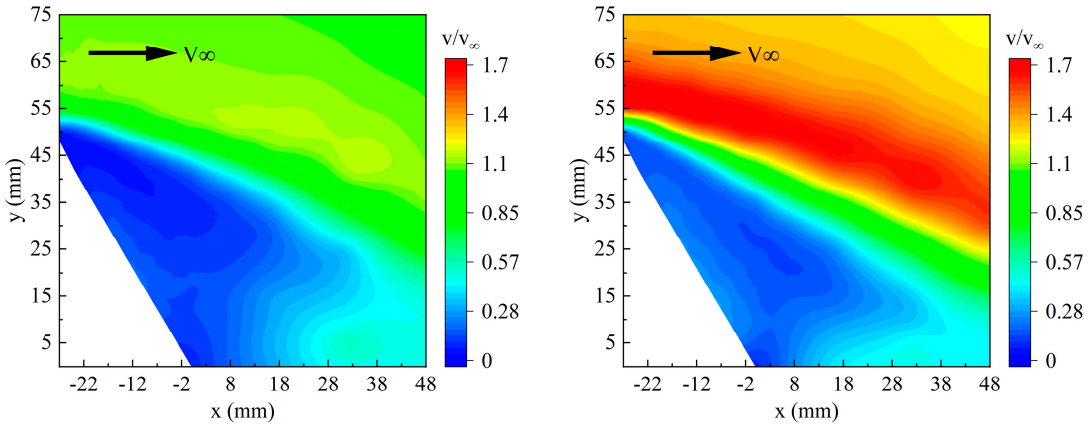


Figure 11. Lift coefficient under different thrust coefficients without jet flow.

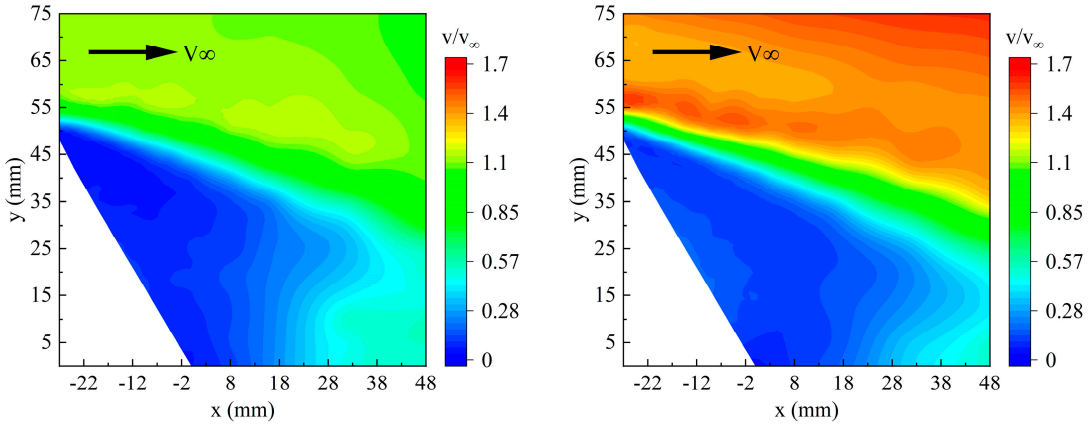
Figure 12 shows the velocity flow field of the wing at different flap positions for thrust coefficients of 0.13 and 0.46. As the thrust coefficient increases, a significant increase in velocity in the mainstream area can be observed, while the changes in the low-speed region are relatively small. For the same thrust coefficient, due to the slipstream's high-speed flow slightly biased toward the downwash side, the local Reynolds number at the flap position increases [25,26]. This helps delay the flow separation over the flap. Comparing the downwash-side section (Section 1) and the upwash-side section (Section 3), the low-speed region on the downwash side is smaller than that on the upwash side, and the separation shear layer has a certain downward deflection. Additionally, at a thrust coefficient of 0.46, for the flap position directly aligned with the propeller (Section 2), the high-speed region in the mainstream area is biased upward. In comparison, Sections 1 and 3 have lower positions for the high-speed region. This is due to the influence of the propeller nacelle, which generates nacelle vortices on both sides of the nacelle as the airflow passes through it [15,27]. These vortices continually absorb the airflow energy near the wall at the nacelle center [27]. Furthermore, because the speed at the propeller's direct position is higher and the leading-edge relative angle of attack is greater, the boundary layer at the trailing-edge flap position becomes thicker, causing the mainstream to shift upward.

3.2. Jet Control Under Slipstream Effect

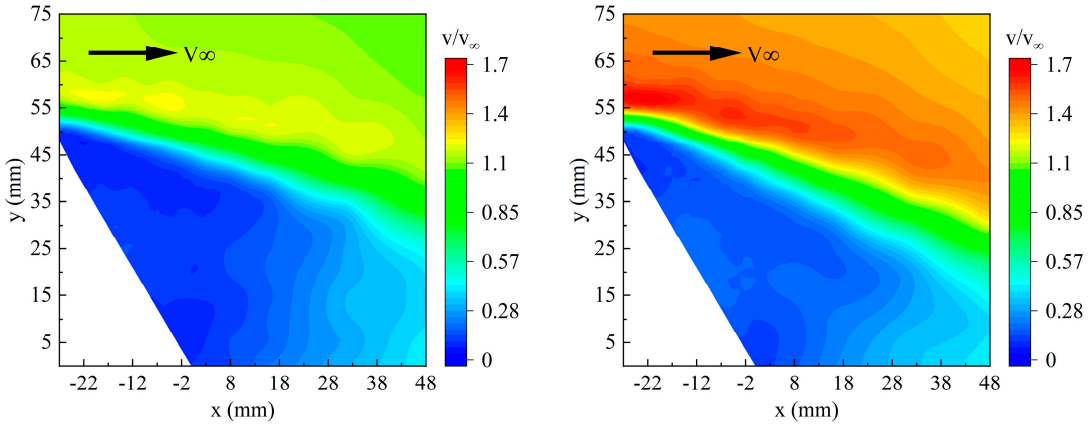
Figure 13a shows the variation of ΔC_L with different momentum coefficients for the uniformly distributed jet of actuator A. It is clearly observed that as the momentum coefficient increases, ΔC_L increases accordingly. Figure 13b shows the corresponding lift gain factor curve. When the momentum coefficient increases to 0.1, the lift gain factor decreases by approximately 65% compared to when the momentum coefficient is 0.01. From theoretical analysis, the jet from the actuator can improve the airflow characteristics on the flap surface. When airflow attachment is enhanced, the flow becomes smoother, thereby increasing the pressure difference between the upper and lower surfaces of the wing and enhancing the lift. However, as the momentum coefficient increases, flow separation at the flap position is completely eliminated. Beyond this point, further increases in the momentum coefficient result in diminishing returns in terms of lift coefficient improvement. Therefore, when the momentum coefficient continues to increase, the lift enhancement coefficient shows a decreasing trend. Additionally, it can be observed that at the same momentum coefficient, a higher thrust coefficient leads to a greater lift enhancement coefficient and lift gain coefficient. This indicates that stronger slipstream effects result in more significant jet flow control effects.



(**a**) Section 1, $C_{T,W}$ = 0.13. (**b**) Section 1, $C_{T,W}$ = 0.46.



(**c**) Section 2, $C_{T,W}$ = 0.13. (**d**) Section 2, $C_{T,W}$ = 0.46.

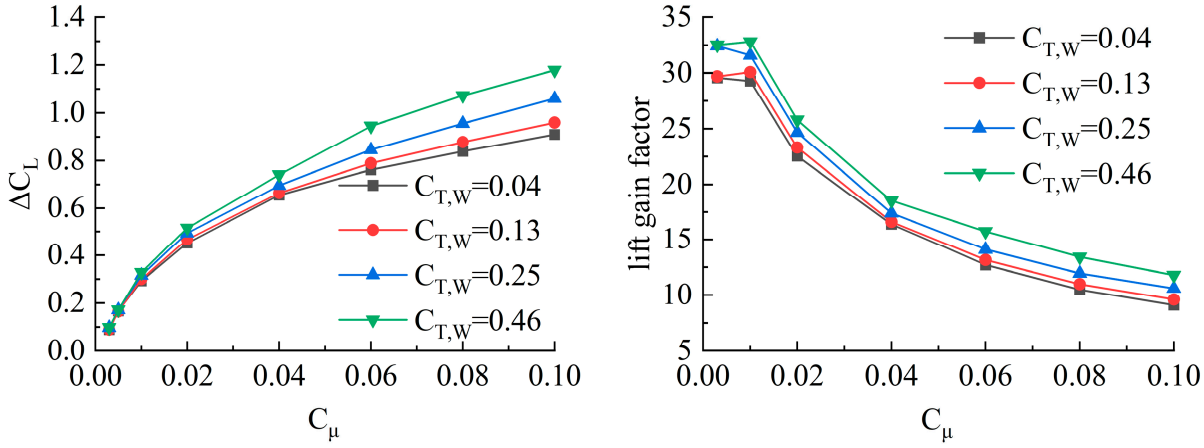


(**e**) Section 3, $C_{T,W}$ = 0.13. (**f**) Section 3, $C_{T,W}$ = 0.46.

Figure 12. The flow field at the flap position without jet flow: (**a**) Section 1, $C_{T,W}$ = 0.13; (**b**) Section 1, $C_{T,W}$ = 0.46; (**c**) Section 2, $C_{T,W}$ = 0.13; (**d**) Section 2, $C_{T,W}$ = 0.46; (**e**) Section 3, $C_{T,W}$ = 0.13; (**f**) Section 3, $C_{T,W}$ = 0.46.

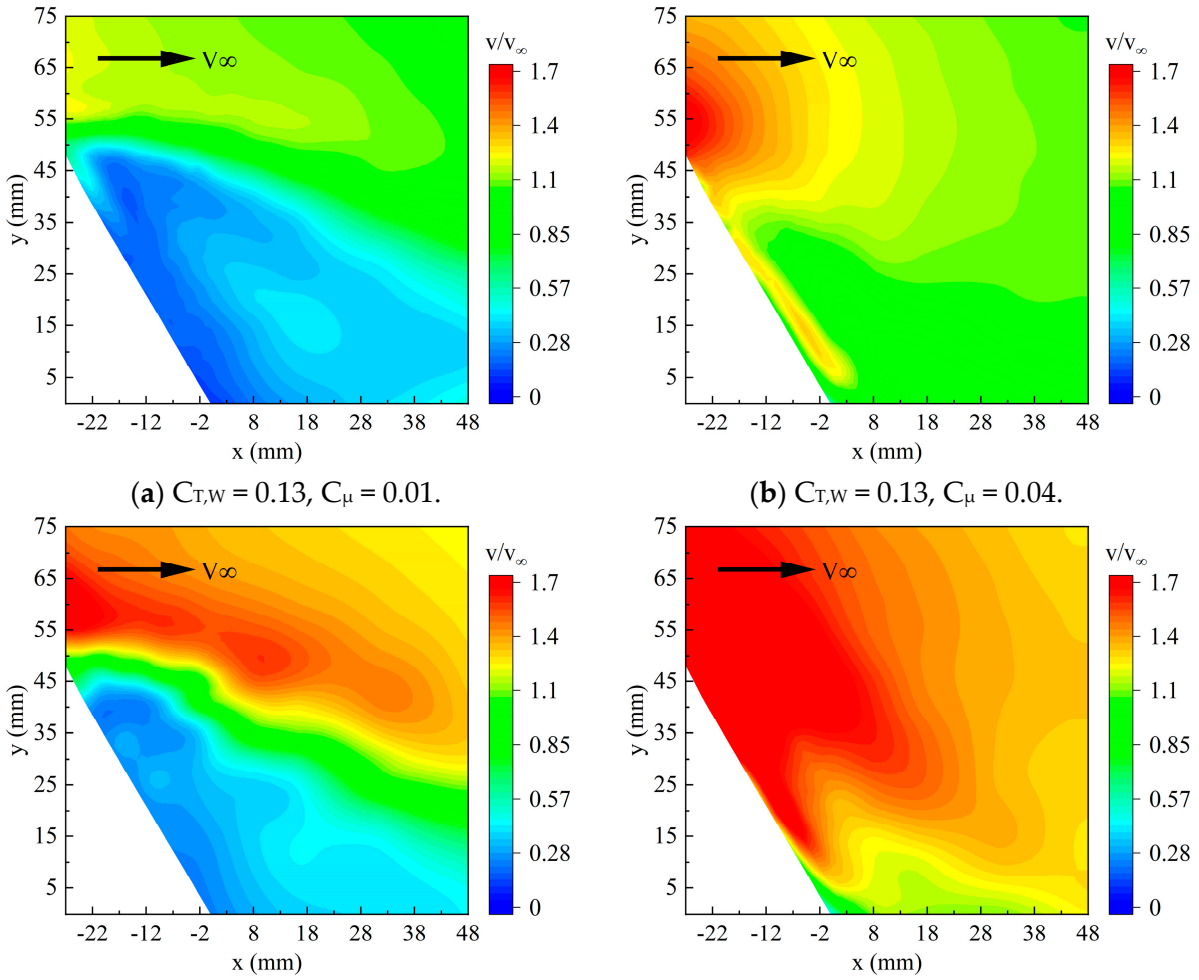
Figure 14 shows the flow field at Section 1 of the downwash-side flap under different momentum coefficients, with thrust coefficients of 0.13 and 0.46. When the momentum coefficient is 0.01, compared to the no-jet control condition in Figure 12, part of the flap separation is eliminated, and the flow speed in the low-speed region is improved to some extent. When the momentum coefficient reaches 0.04, separation at the flap is completely controlled. When comparing the same momentum coefficient, a higher thrust coefficient results in a larger dynamic pressure in the mainstream region, leading to better control effects and therefore a higher lift enhancement. The slipstream effect reduces the effective

angle of attack on the downwash side, which results in a slight reduction in lift. However, the propeller's acceleration effect increases the lift, ultimately leading to a significant increase in the lift on the downwash side.



(**a**) Lift enhancement coefficient. (**b**) Lift gain factor.

Figure 13. Lift enhancement coefficient and lift gain factor under different momentum coefficients.

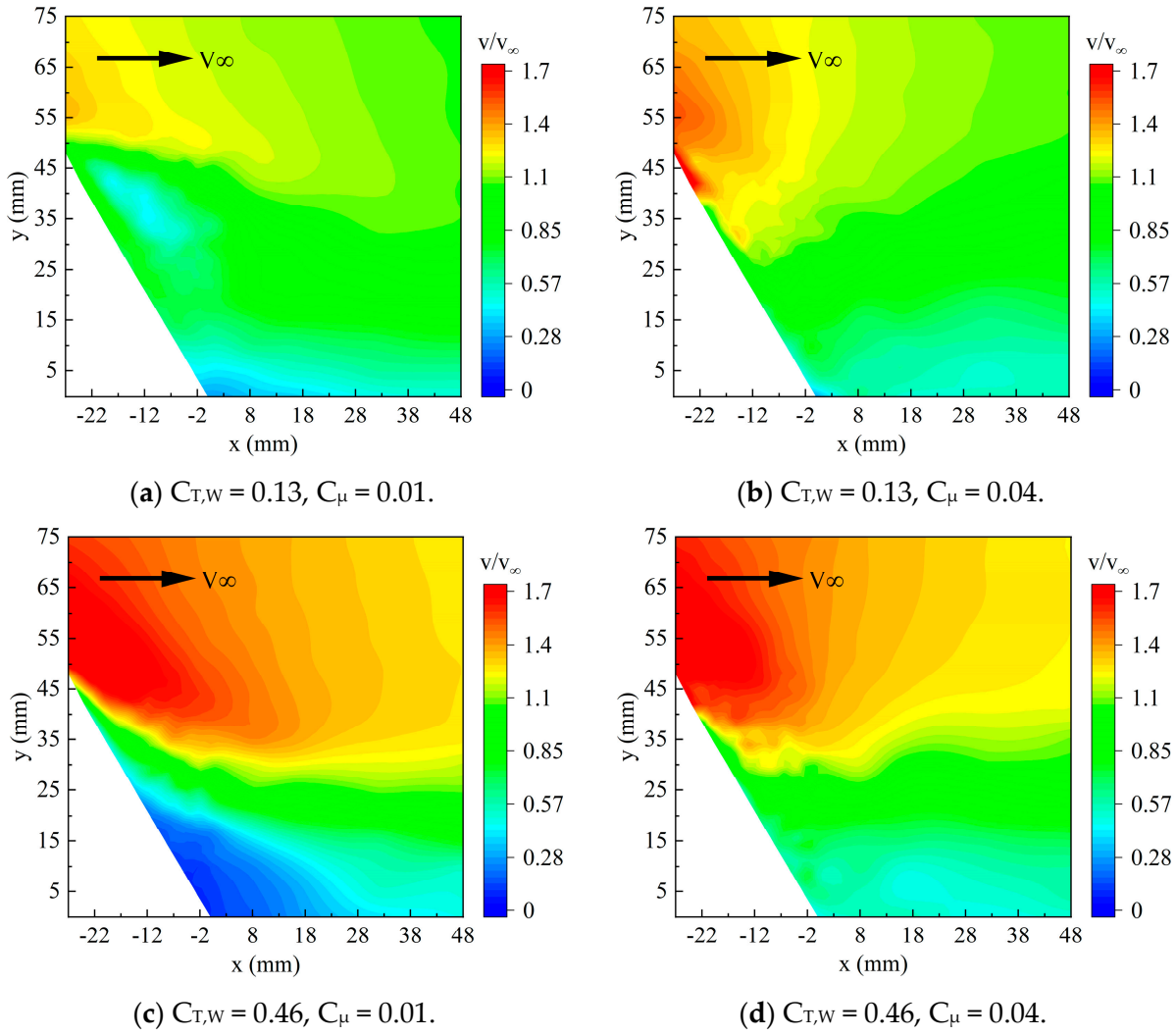


(**a**) $C_{T,W}$ = 0.13, C_μ = 0.01. (**b**) $C_{T,W}$ = 0.13, C_μ = 0.04.

(**c**) $C_{T,W}$ = 0.46, C_μ = 0.01. (**d**) $C_{T,W}$ = 0.46, C_μ = 0.04.

Figure 14. Flow field at Section 1 under different momentum coefficients: (**a**) $C_{T,W}$ = 0.13, C_μ = 0.01; (**b**) $C_{T,W}$ = 0.13, C_μ = 0.04; (**c**) $C_{T,W}$ = 0.46, C_μ = 0.01; (**d**) $C_{T,W}$ = 0.46, C_μ = 0.04.

The flow field at Section 3 on the upwash-side flap is shown in Figure 15. At low momentum coefficients, Section 3 demonstrates a significant control effect. When the momentum coefficient reaches 0.04, flap separation is completely eliminated. The upwash airflow from the propeller provides additional flow acceleration in the flap region, increasing the flow speed near the flap surface. This enhancement increases the lift effect on the flap, effectively reducing the risk of flow separation and improving the airflow stability in the flap region.



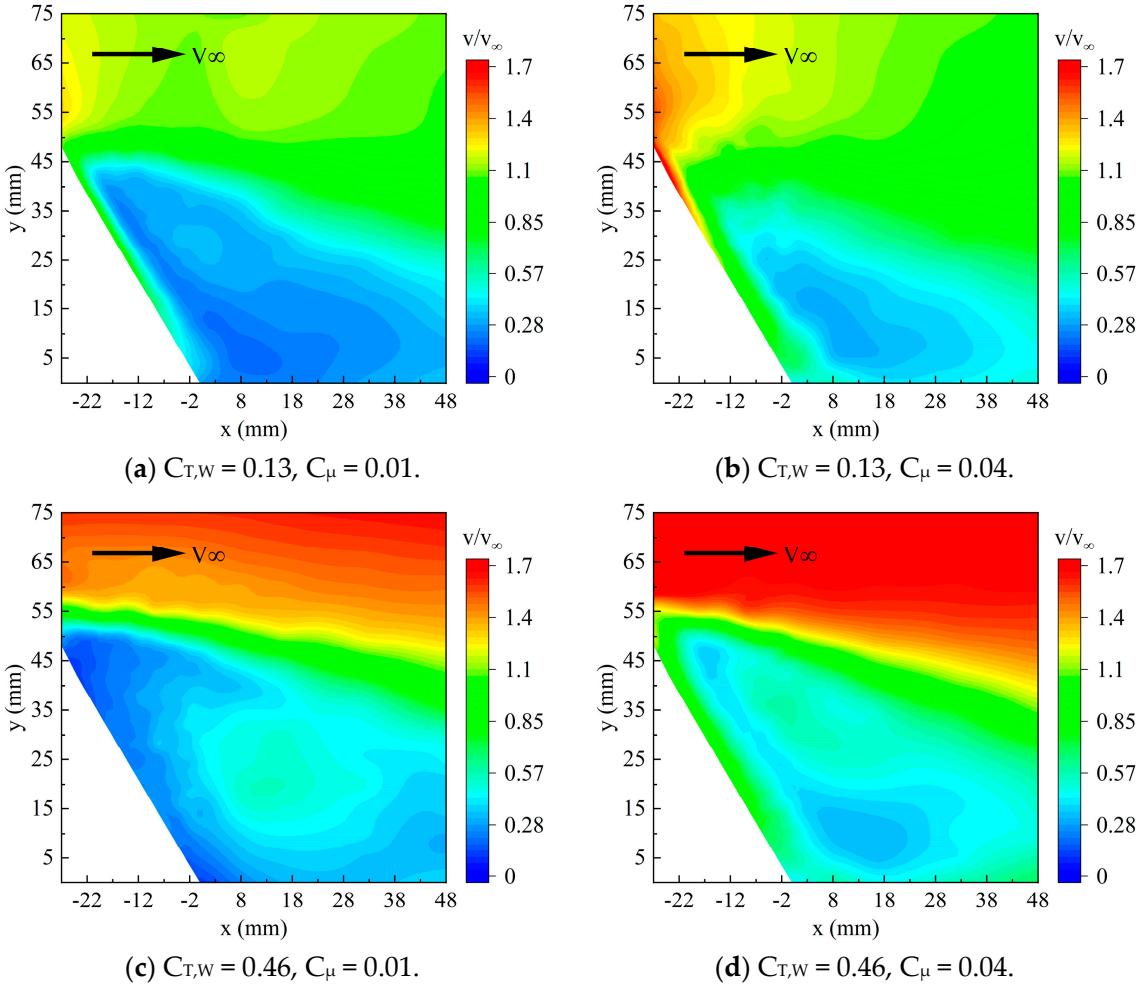
(**a**) $C_{T,W}$ = 0.13, C_μ = 0.01. (**b**) $C_{T,W}$ = 0.13, C_μ = 0.04.

(**c**) $C_{T,W}$ = 0.46, C_μ = 0.01. (**d**) $C_{T,W}$ = 0.46, C_μ = 0.04.

Figure 15. Flow field at Section 3 under different momentum coefficients. (**a**) $C_{T,W}$ = 0.13, C_μ = 0.01; (**b**) $C_{T,W}$ = 0.13, C_μ = 0.04; (**c**) $C_{T,W}$ = 0.46, C_μ = 0.01; (**d**) $C_{T,W}$ = 0.46, C_μ = 0.04.

As shown in Figure 16, the flow field at Section 2, which is directly in front of the propeller, is depicted after the increase in jet momentum. It is evident that the improvement in the flow field at the propeller's directly aligned position with increasing momentum coefficients is less pronounced than at the upwash and downwash sides. Compared to the case without jet flow control, when the momentum coefficient reaches 0.01, the separation region and mainstream flow speed show slight improvement, and the shear layer moves downward. When the jet momentum increases to 0.04, a clear reduction in separation can be observed in the flow field. However, unlike Sections 1 and 3, it is observed that while the jet flow attaches to the flap, a low-speed region appears between the jet and mainstream flow, resulting in spatial separation. This indicates that to completely eliminate separation, more jet momentum is required than at Sections 1 and 3. The reason for this can be analyzed: at low jet momentum, the jet flow accelerates the surrounding air,

"attracting" the mainstream flow towards the flap. This phenomenon causes an increase in the mainstream flow speed, essentially attracting higher-positioned airflow to attach to the flap. When the jet momentum coefficient is increased to 0.04, due to the difference in kinetic energy between the jet and mainstream flow, as well as the differing jet angle and mainstream direction, vortices or turbulence are generated by the jet flow. This mixing process leads to the formation of a localized low-speed region between the jet flow and incoming flow.



(**a**) $C_{T,W}$ = 0.13, C_μ = 0.01. (**b**) $C_{T,W}$ = 0.13, C_μ = 0.04.

(**c**) $C_{T,W}$ = 0.46, C_μ = 0.01. (**d**) $C_{T,W}$ = 0.46, C_μ = 0.04.

Figure 16. Flow field at Section 2 under different momentum coefficients. (**a**) $C_{T,W}$ = 0.13, C_μ = 0.01; (**b**) $C_{T,W}$ = 0.13, C_μ = 0.04; (**c**) $C_{T,W}$ = 0.46, C_μ = 0.01; (**d**) $C_{T,W}$ = 0.46, C_μ = 0.04.

3.3. Control Effect of Local Momentum Change Under Slipstream Effect

Under the influence of the propeller slipstream effect, the slipstream velocity along the spanwise direction of the wing is not uniform. The wing surface at the propeller's directly aligned position experiences much stronger slipstream intensity than at the wing tips. As discussed earlier, the flow field indicates that for an actuator with a uniformly distributed spanwise jet, the flow separation at the flap directly in front of the propeller is more severe than on the sides. Higher jet momentum is needed to completely eliminate flap separation in this region. Actuator A has a uniformly distributed spanwise jet with consistent momentum distribution. Based on actuator A, without changing the slot height, the local jet slot area of the actuator can be reduced by adding a blockage. This modification aims to adjust the local jet momentum coefficient by decreasing the area of the jet slot, allowing for better control of the flow characteristics and potentially improving the overall jet control effectiveness in certain regions.

Figure 17 shows the curves of the lift coefficient variation with the momentum coefficient for different actuators. As the momentum coefficient and thrust coefficient change, actuator B (with the jet slot area at the propeller's directly aligned position being 1.5 times that of the sides) consistently demonstrates the best lift enhancement capability. The next most effective actuators are D (with the downwash-side jet slot area being 1.5 times that of the upwash side) and E (with the upwash-side jet slot area being 1.5 times that of the downwash side). Since the upwash and downwash sides are distinguished by the propeller centerline, this results in each side having half of the jet slots located at the propeller's directly aligned position. Actuators D and E increase the momentum coefficient at the propeller's directly aligned position, leading to better performance compared to actuators A and C (where the jet slot area at the sides is 1.5 times that of the propeller's directly aligned position). When the thrust coefficient is 0.13, 0.25, and 0.46, actuator B improves the lift effect by 35.5%, 41.3%, and 52.6%, respectively, compared to actuator A. This indicates that as the thrust coefficient increases, the control effect of actuator B becomes more significant. Due to the slipstream direction being biased towards the downwash side, actuator D shows better control performance than actuator E when the slipstream effect strengthens. Additionally, actuator C, which distributes more momentum to the sides, consistently shows the poorest control performance. Figure 18 shows the lift augmentation coefficient curves under different thrust coefficients at the same momentum coefficient. It can be observed that as the thrust coefficient increases, the lift augmentation coefficient also increases, indicating that the enhancement of slipstream effects can improve the lift of the airfoil. Actuator B consistently exhibits the highest lift augmentation coefficient, reflecting the rationality of allocating more momentum at the position directly opposite the propeller.

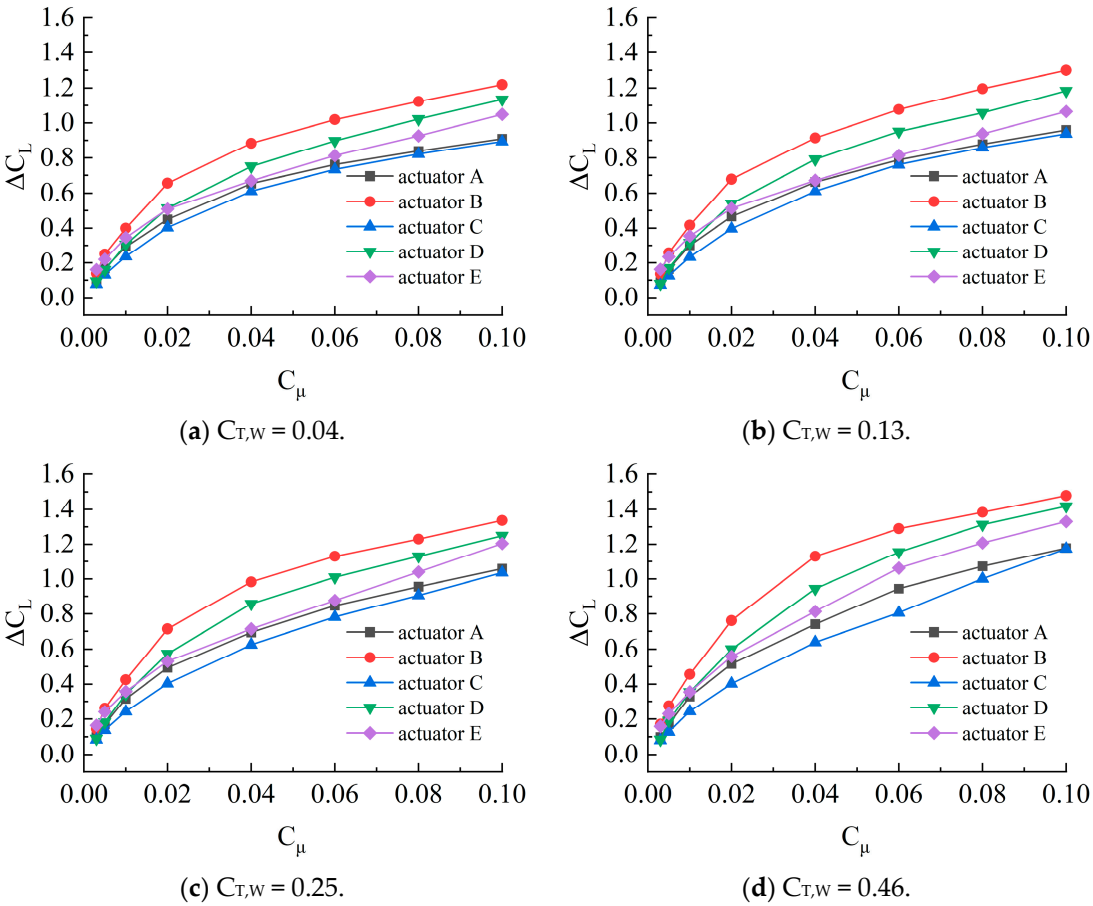


Figure 17. The lift augmentation coefficient of different actuators: (**a**) $C_{T,W}$ = 0.04; (**b**) $C_{T,W}$ = 0.13; (**c**) $C_{T,W}$ = 0.25; (**d**) $C_{T,W}$ = 0.46.

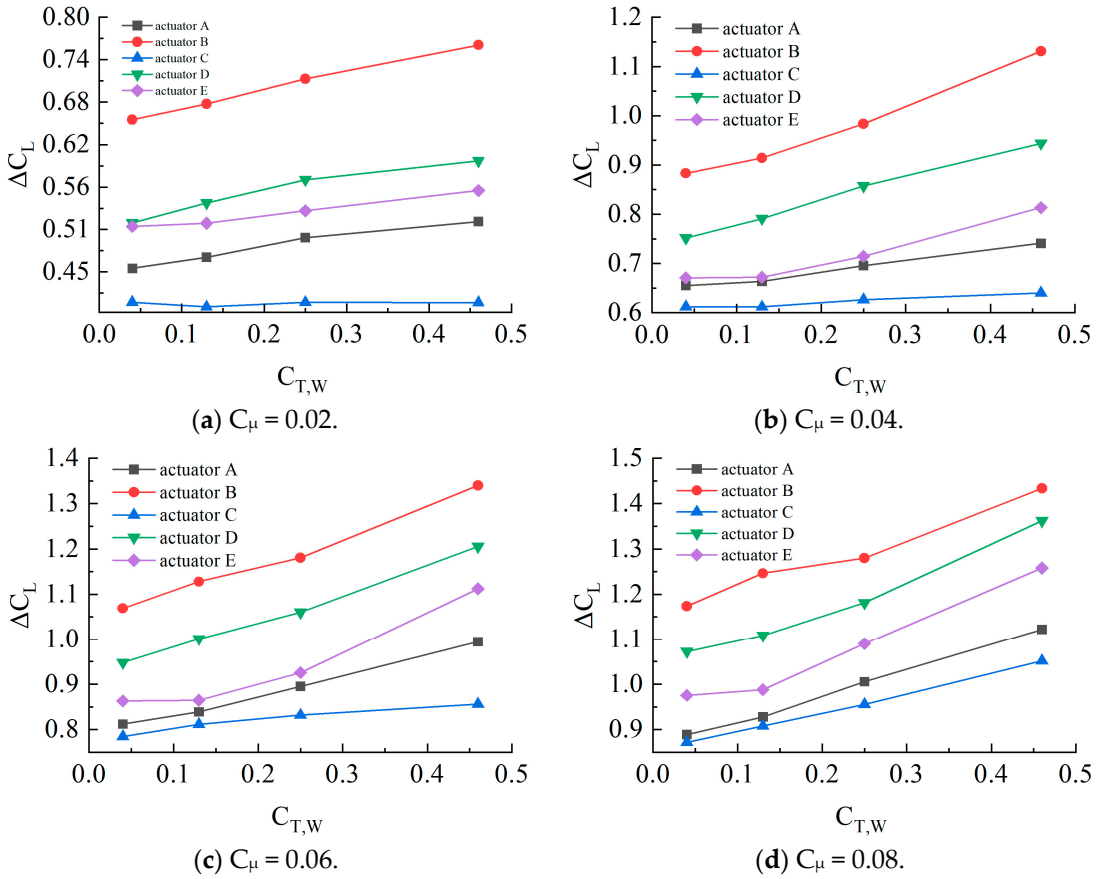
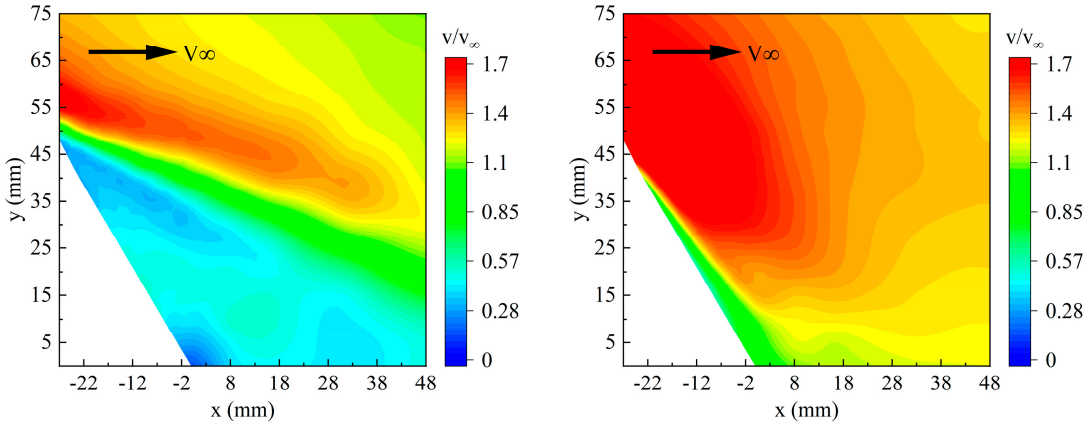


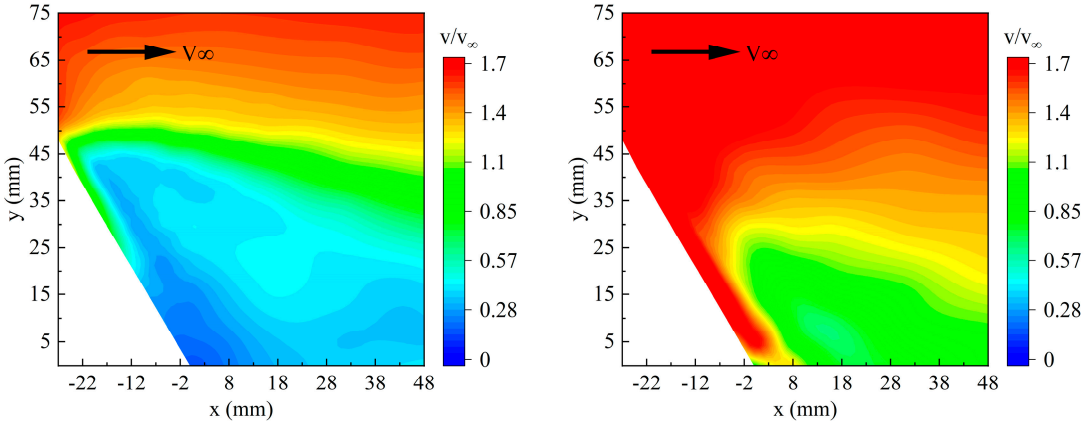
Figure 18. The lift augmentation coefficient of different actuators: (**a**) C_μ = 0.02; (**b**) C_μ = 0.04; (**c**) C_μ = 0.06; (**d**) C_μ = 0.08.

From the performance of these five different actuators, we can conclude that for wings affected by the propeller slipstream effect, setting a localized high momentum coefficient at the propeller's directly aligned position can effectively improve the lift enhancement effect while also requiring less overall jet flow.

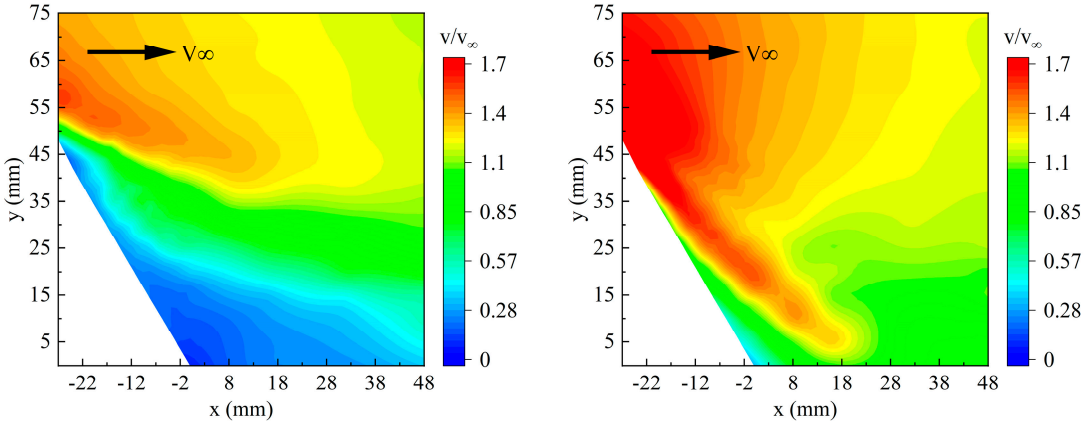
Figure 19 shows the flow field at the flap's Section 2 for actuator B with a thrust coefficient of 0.46. From the flow field, we can clearly observe the jet control effect of actuator B at Section 2 of the flap. Comparing with Figure 16c,d, when the jet momentum coefficient is 0.01, actuator B not only reduces the separation region compared to actuator A but also increases the speed in the mainstream region. When the jet momentum coefficient increases to 0.04, actuator B nearly completely controls the separation at Section 2 of the flap, while actuator A still shows a noticeable separation region. When the jet momentum coefficient is increased to 0.06, actuator A nearly completely controls the separation at Section 2, but visually, the control effect is still not as effective as that of actuator B at a momentum coefficient of 0.04. When comparing the flow fields at the upwash and downwash sides for actuator A and actuator B with a jet momentum coefficient of 0.04, we can see that separation at the flap is effectively controlled in both cases. To maintain a consistent overall jet momentum coefficient, actuator B essentially increases the jet momentum coefficient at the propeller's directly aligned position while reducing the jet momentum coefficients at the sides. In fact, the slipstream velocity at the sides is lower than at the center, and the influence of the propeller blades and the short nacelle on the incoming flow is also less. Therefore, smaller jet momentum compared to the center position is sufficient to completely control flap separation. This is why actuator B can effectively control separation at the propeller's directly aligned position while also achieving good control over the separation regions at both sides of the flap.



(**a**) Section 1, $C_{T,W}$ = 0.46, C_μ = 0.01. (**b**) Section 1, $C_{T,W}$ = 0.46, C_μ = 0.04.



(**c**) Section 2, $C_{T,W}$ = 0.46, C_μ = 0.01. (**d**) Section 2, $C_{T,W}$ = 0.46, C_μ = 0.04.



(**e**) Section 3, $C_{T,W}$ = 0.46, C_μ = 0.01. (**f**) Section 3, $C_{T,W}$ = 0.46, C_μ = 0.04.

Figure 19. The flow field at different sections of the flap: (**a**) Section 1, $C_{T,W}$ = 0.46, C_μ = 0.01; (**b**) Section 1, $C_{T,W}$ = 0.46, C_μ = 0.04; (**c**) Section 2, $C_{T,W}$ = 0.46, C_μ = 0.01; (**d**) Section 2, $C_{T,W}$ = 0.46, C_μ = 0.04; (**e**) Section 3, $C_{T,W}$ = 0.46, C_μ = 0.01; (**f**) Section 3, $C_{T,W}$ = 0.46, C_μ = 0.04.

4. Discussion

This paper investigates the influence of the coupling effects of propeller slipstream and jet flow on airfoil lift. While early studies separately explored the effects of propeller slipstream and jet flow on airfoil lift, they did not explicitly discuss the impact of different jet flow distribution methods on airfoil lift under the influence of propeller slipstream.

We found that while the slipstream effect can enhance airfoil lift, it makes it more difficult for airflow to adhere to the flap regions strongly influenced by the slipstream. Typically, the area directly opposite the propeller is most affected by the slipstream, and

the presence of the propeller nacelle leads to the generation of nacelle vortices, making the flow field in this flap region more complex. Flap jet technology can effectively eliminate flap separation. In previous studies, a spanwise uniform jet design method was commonly used. However, this is clearly unsuitable for propeller airfoils, as the flap regions with stronger slipstream effects require more momentum input to completely eliminate flap separation. Our experimental study validated the feasibility of momentum distribution. By allocating the jet momentum from both sides to the jet at the position directly opposite the propeller, we achieved the elimination of global flap separation and realized efficient lift enhancement.

The research results of this paper can provide technical references for aircraft design, especially for short takeoff and landing (STOL) and vertical takeoff and landing (VTOL) aircraft. However, there are certain limitations. Firstly, this study focuses on specific operating conditions with high flap deflection angles and lacks research on freestream velocity and angle of attack variations. Secondly, this paper emphasizes experimental research and lacks mutual validation with numerical simulations. These issues will be further addressed in the next steps of our work. In practical applications, the design of jet momentum distribution increases the complexity of engineering design. Achieving precise momentum distribution inevitably involves challenges related to the installation space of actuators and the distribution of air ducts. Further research is needed to explore how to design compact distribution pipelines and actuators.

5. Conclusions

The lift coefficient and flap flow field analyses were conducted for actuators with different momentum distribution methods under varying jet momentum coefficients. Under the condition of natural incoming flow, the coupling effect of propeller slipstream and jet flow on wing lift was studied. By optimizing the jet flow distribution, the lift enhancement effect under slipstream was significantly improved. When the thrust coefficient was 0.46 and the momentum coefficient was 0.1, the lift increase was 52.6% higher compared to the spanwise uniform jet flow distribution while saving approximately 9% of the jet flow rate. This provides a more comprehensive design approach for future research and applications. The following conclusions were drawn.

The propeller nacelle and blades introduce disturbances to the natural incoming flow, generating vortices on the sides of the nacelle. These vortices, known as nacelle vortices, influence the airflow at the center of the wing, particularly at the propeller's directly aligned position. As a result, the airflow in this region is more disrupted compared to the airflow on the sides of the wing, making the flow at the flap more susceptible to separation.

An increase in the thrust coefficient accelerates the airflow, which helps increase the local angle of attack, thereby improving the overall lift coefficient. After implementing jet flow control, the wing's lift coefficient increases further, and the lift coefficient rises as the jet momentum coefficient increases. The slipstream has a significant impact on the effectiveness of jet flow control. In the high-speed region of the slipstream, more jet momentum is required to completely eliminate flap separation compared to the low-speed region, but this also results in a higher lift coefficient.

Since the slipstream velocity is strongest at the propeller-aligned position, increasing the jet momentum at the center position results in a much greater lift coefficient improvement compared to the wing's sides. For jet flow control lift enhancement designs for wings with propellers, the focus should be on increasing the jet momentum at the propeller-aligned position, followed by the downwash side.

Author Contributions: Conceptualization, Y.S. and W.W.; methodology, Y.S.; software, J.P.; validation, Y.S., J.S. and W.C.; formal analysis, Y.S.; investigation, W.C.; resources, J.S.; data curation, Y.S.; writing—original draft preparation, Y.S. and J.P.; writing—review and editing, Y.S.; visualization, X.Z.; supervision, X.Z.; project administration, W.W.; funding acquisition, W.W. All authors have read and agreed to the published version of the manuscript.

Funding: This research received no external funding.

Data Availability Statement: Data are contained within the article.

Conflicts of Interest: The authors declare no conflicts of interest.

References

1. Zeune, C. An overview of the Air Force's speed agile concept demonstration program. In Proceedings of the 51st AIAA Aerospace Sciences Meeting including the New Horizons Forum and Aerospace Exposition, Grapevine, TX, USA, 7–10 January 2013; p. 1097.
2. Burnazzi, M.; Radespiel, R. Design and analysis of a droop nose for coanda flap applications. *J. Aircr.* **2014**, *51*, 1567–1579. [CrossRef]
3. Beck, N.; Radespiel, R.; Lenfers, C.; Friedrichs, J.; Rezaeian, A. Aerodynamic effects of propeller slip-stream on a wing with circulation control. *J. Aircr.* **2015**, *52*, 1422–1436. [CrossRef]
4. Zhang, Q.; Wang, Z.; Wei, M.; Lin, W. Overview of Special Design of Lift Augmentation Devices for Large Amphibious Aircraft. *J. Aerodyn.* **2019**, *37*, 19–32.
5. Gong, Z.; Li, J.; Jiang, S.; Zhang, H. Numerical Simulation of Power Augmentation Jet Flow Effect for Large Transport Aircraft. *J. Aerosp. Power* **2016**, 1811–1819. [CrossRef]
6. Wang, M.; Sun, W.; Qin, H. Optimization Design of Inward-Blowing Flaps for Amphibious Aircraft. *Acta Aeronaut. Astronaut. Sin.* **2016**, *37*, 300–309.
7. Alba, C.; Elham, A.; German, B.J.; Veldhuis, L.L. A surrogate-based multi-disciplinary design optimization framework modeling wing–propeller interaction. *Aerosp. Sci. Technol.* **2018**, *78*, 721–733. [CrossRef]
8. Miranda, L.; Brennan, J. Aerodynamic effects of wingtip-mounted propellers and turbines. In Proceedings of the 4th Applied Aerodynamics Conference, San Diego, CA, USA, 9–11 June 1986; p. 1802.
9. Rakshith, B.R.; Deshpande, S.M.; Narasimha, R.; Praveen, C. Optimal low-drag wing planforms for tractor-configuration propeller-driven aircraft. *J. Aircr.* **2015**, *52*, 1791–1801. [CrossRef]
10. Veldhuis, L.L.M.; Heyma, P.M. Aerodynamic optimization of wings in multi-engined tractor propeller arrangements. *Aircr. Des.* **2000**, *3*, 129–149. [CrossRef]
11. Veldhuis, L.L.M. Optimization of tractor propeller/wing configurations. *Proc. Inst. Mech. Engneers Part G J. Aerosp. Eng.* **1995**, *209*, 215–226. [CrossRef]
12. Veldhuis, L.L.M. Review of propeller-wing aerodynamic interference. In Proceedings of the 24th International Congress of the Aeronautical Sciences, Edinburgh, UK, 29 August–3 September 2004; Optimage Ltd.: Edinburgh, UK, 2004; Volume 6, p. 2004-6.3.
13. Xue, C.; Zhou, Z. Propeller-wing coupled aerodynamic design based on desired propeller slipstream. *Aerosp. Sci. Technol.* **2020**, *97*, 105556. [CrossRef]
14. Ma, S.; Wang, J.; Qiu, M.; Liu, G. Unsteady Numerical Simulation Verification of Slipstream Effects on Propeller Aircraft. *J. Aerodyn.* **2019**, *37*, 804–812.
15. Keller, D.; Rudnik, R. Numerical investigations of aerodynamic properties of a propeller blown circulation control system on a high wing aircraft. *CEAS Aeronaut. J.* **2016**, *7*, 441–454. [CrossRef]
16. Murnieks, V.A.; Spens, A.; Heidersbach, R.; Seth, D. Wing Trailing Edge Coanda Flow Control; Effect of Actuator Placement Relative to Up-stream Propeller Slipstream. In Proceedings of the AIAA SCITECH 2024 Forum, Orlando, FL, USA, 8–12 January 2024; p. 0696.
17. Murnieks, V.A.; Spens, A.; Heidersbach, R.; Seth, D. Effectiveness of Various Trailing Edge Coanda Actuator Nozzles and Surfaces with a Propeller Slipstream Flow. In Proceedings of the AIAA SCITECH 2024 Forum, Orlando, FL, USA, 8–12 January 2024; p. 0697.
18. Chard, J.; Llopis-Pascual, A.; Crowther, W. Plenum design for compact fluidic effectors. In Proceedings of the 33rd AIAA Applied Aerodynamics Conference, Dallas, TX, USA, 22–26 June 2015; p. 3314.
19. Crowther, B.; Nabawy, M.; Penty Geraets, R.; Nabawy, M. DARPA CRANE–A toolset for the design of compact fluidic distribution systems for flow control applications: Part 1–model development and system optimization. In Proceedings of the AIAA SCITECH 2023 Forum, Oxon Hill, MD, USA, 23–27 January 2023; p. 2311.

20. Crowther, B.; Shearwood, T.R.; Nabawy, M.; Penty Geraets, R.; Quinn, M.K.; Weigert, S.; Warsop, C.; Forster, M.; Axani, L. DARPA CRANE–A toolset for the design of compact fluidic distribution systems for flow control applications: Part 2–model validation and implementation. In Proceedings of the AIAA SCITECH 2023 Forum, Oxon Hill, MD, USA, 23–27 January 2023; p. 2312.
21. Liu, R.; Bai, J.; Qiu, Y.; Gao, G. Study on the Influence and Optimization Design of Geometric Parameters of Internal Blown Flaps. *J. Northwestern Polytech. Univ.* **2020**, *38*, 58–67. [CrossRef]
22. Catalano, F.M. On the effects of an installed propeller slipstream on wing aerodynamic characteristics. *Acta Polytech.* **2004**, *44*, 8–14. [CrossRef] [PubMed]
23. Fu, W.; Li, J.; Wang, H. Numerical simulation of propeller slipstream effect on a propeller-driven unmanned aerial vehicle. *Procedia Eng.* **2012**, *31*, 150–155. [CrossRef]
24. Bouquet, T.; Vos, R. Modeling the propeller slipstream effect on lift and pitching moment. In Proceedings of the 55th AIAA Aerospace Sciences Meeting, Grapevine, TX, USA, 9–13 January 2017; p. 0236.
25. Lenfers, C.; Beck, N.; Radespiel, R. Numerical and experimental investigation of propeller slipstream interaction with active high lift wing. In Proceedings of the 35th AIAA Applied Aerodynamics Conference, Denver, CO, USA, 5–9 June 2017; p. 3248.
26. Yang, X.; Wang, Y.; Wang, G.; Zhang, Y. Efficient Numerical Simulation of Unsteady Slipstream of Propellers. *J. Aerodyn.* **2014**, *32*, 289–294.
27. Wen, Q.; Yang, K.; Wei, M.; Cheng, Z.; Jia, Z. Study on the Stall Reduction of Propeller Aircraft with Short Nacelle Vortex Generators. *J. Aerosp. Power* **2023**, *38*, 2610–2617.

Disclaimer/Publisher's Note: The statements, opinions and data contained in all publications are solely those of the individual author(s) and contributor(s) and not of MDPI and/or the editor(s). MDPI and/or the editor(s) disclaim responsibility for any injury to people or property resulting from any ideas, methods, instructions or products referred to in the content.